

Part I

Some Approaches to Quantitative Dendritic Morphology

Robert E. Burke and William B. Marks

“If ye canna mak a model, then ye dinna understand it.”
(Attributed to Lord Kelvin)

ABSTRACT

The availability of powerful desktop computers and of a large amount of detailed data about the morphology of a wide variety of neurons has led to the development of computational approaches that are designed to synthesize such data into biologically meaningful patterns. The hope is, of course, that the emerging patterns will provide clues to the factors that control the formation of neuronal dendrites during development, as well as their maintenance in the adult animal. One class of approaches to this problem is to develop quantitative computational models that can reproduce as many aspects of the original data as possible. The development of such simulations requires analysis of the original data that is directed by the model requirements, and their relative success depends on detailed comparisons between model outputs and the original data sets. Refinement of the models may require not only new experiments, as in other scientific disciplines, but also new ways of looking at the data already in hand. This chapter discusses some examples of this process, with emphasis on spinal motoneurons.

2.1. INTRODUCTION

Dendrites are critical to the processing of synaptic information in central nervous system neurons. Accordingly, there is considerable interest in their structure and function (1). Striking differences in neuron morphologies have been known for over a century (2,3). Such differences must be related to factors that govern the development and maintenance of their dendritic architectures. Over the past two decades, the development of intracellular labeling techniques using horseradish peroxidase (HRP) and biocytin (4,5), combined with computer-assisted methods for quantitative reconstruction of labeled neurons (6,7), have led to a large output of quantitative data about the morphology of dendrites. We now face the problem of how to reduce the mass of information, usually contained in multiple graphs and tables, into patterns that reveal their

underlying meaning, without losing essential information. Hillman (8) called these patterns “fundamental parameters of form”, but the underlying factors that produce them are not obvious upon inspection of the raw data. This chapter considers some approaches to this problem.

Two issues require some comment before proceeding. First, it has become clear in recent years that neuronal dendrites are not static structures; rather they can exhibit dynamic changes that presumably reflect functional changes in the nervous system (9). Thus, the data about dendritic structure that are obtained by conventional neuroanatomical methods represent snapshots that may not be entirely representative. Second, there are a large number of practical difficulties inherent in gathering quantitative measurements of neuronal dendrites using conventional light microscopy (see [10]). These include factors such as tissue shrinkage, operator error, and the limited resolution of the light microscope, which is the only practical approach to reconstructing large neurons from serial sections. These sources of potential error must be kept firmly in mind when evaluating existing data, particularly when data from different sources are combined. Other options such as confocal microscopy of neurons filled with fluorescent tracers could, in principle, be more accurate and might even contribute an element of automation to the reconstruction process. However, technical problems, such as tracer bleaching, have confined most reconstruction efforts to more permanent forms of tracers, like HRP or biocytin, to be examined with conventional light microscopy.

With regard to data analysis, it is also important to remember that the process of quantitative reconstruction splits the continuous structure of the dendrite into discrete pieces, here referred to as “segments”, each with a specified diameter and length. These discrete cylinders, plus information that identifies their positions within the dendritic tree, make up the usual computer data files. The position coding systems often vary between data sources, as does the presence or absence of information about the 3D location of each cylinder.

2.2. TWO-DIMENSIONAL ANALYSIS OF DENDRITES IN ISOLATED NEURONS

Quantitative analysis of neuronal dendrites began before the age of computers with the work of Sholl (11), who plotted dendritic branching patterns of Golgi-stained cortical neurons in terms of distance from the soma. This straightforward approach guided many subsequent studies that used improved methods for intracellular staining of identified neurons, resulting in ever larger volumes of quantitative data about branch diameters and lengths, branching orders, and the locations of branching points and terminations, all considered as functions of distance from the soma (e.g., Fig. 1; see also [12,13]). An alternative approach, focused on dendritic branching patterns *per se*, concentrates on the topological complexity of trees from different types of neurons (14–16) (see Chapter 11). Neither approach takes account of the 3D tree structures.

Hillman (8,17) proposed that dendritic architecture can provide clues to the biological factors that control the multiplicity of neuronal shapes. Hillman’s seven fundamental parameters that describe the morphology of a dendritic tree are: (i) stem diameter; (ii) terminal branch diameters; (iii) branch taper; (iv) branch lengths; (v) branch power (the relation between diameters of the parent branch with those of its two daughters);

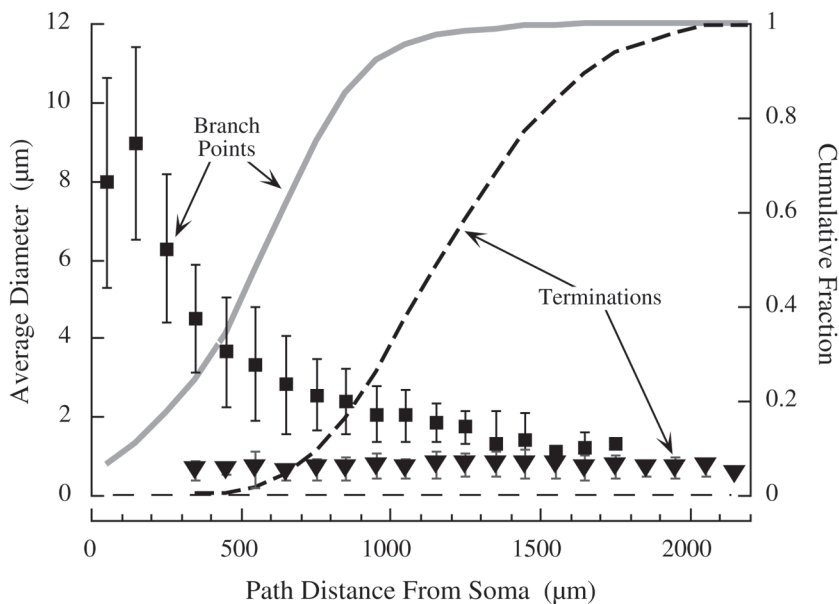


Fig. 1. Some features of cat α -motoneuron dendrites plotted as functions of the somatofugal distance along dendritic paths (abscissa). The solid and dashed lines show the locations of branching points and terminations, respectively, as cumulative fractions. The symbols indicate the average diameters (\pm one SD) of all branches that end in branching points (parent branches; solid squares) or terminations (solid triangles) within 100 μm bins of path distance. Data from 6 cat lumbosacral motoneurons reported in (12).

(vi) the ratio of the two daughter branch diameters at each branch point; and (vii) the spatial orientation of branches. Hillman suggested that the cytoskeleton, particularly microtubule arrays, is critical to the control of dendritic architecture (17) (but cf [18]). The interrelations that he described implied that some combination of intrinsic factors could be used to simulate virtual dendrites that could be compared with real ones. It seemed possible that some correlation, which may be found among the descriptors, may arise as epiphenomena that depend on underlying mechanisms (see also [19]).

Building on this idea, we proposed an approach to this problem that began by analyzing correlations in quantitative data about completely reconstructed dendritic trees of a sample of cat α -motoneurons, in order to develop algorithms and appropriate data sets that might be used to construct virtual dendrite simulations (20). We reasoned that a computational machine (algorithms plus parameters), which can construct virtual dendrites that reproduce not only the averages but also the variances of data from actual neurons, must contain all of the essential information inherent in that data set (see also [21]). There are a large number of correlations to choose from, and several different approaches were explored. All used a Monte Carlo simulation in order to generate the stochastic variations found in the observations.

The most successful algorithm was based on the relationship between the starting diameter and the length of dendritic branches, which are defined as beginning with the

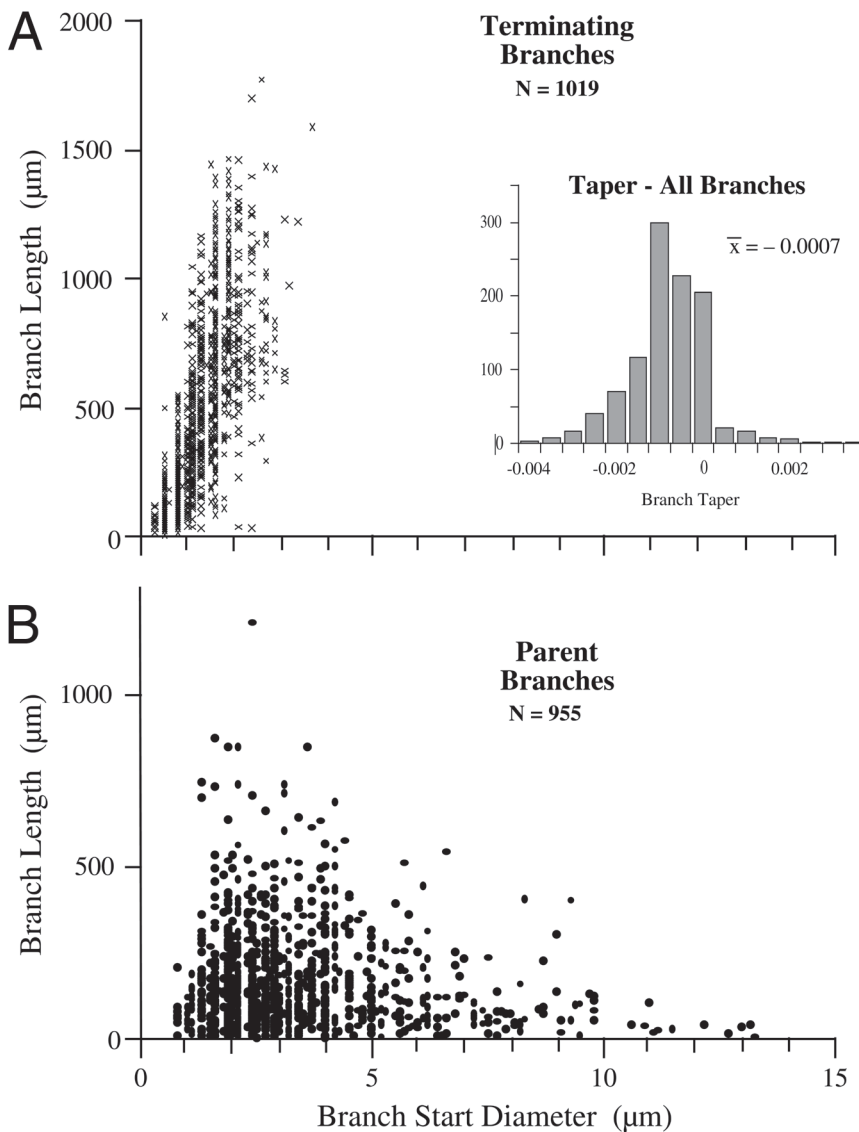


Fig. 2. Scatter plots of the lengths (ordinates) of terminating (**A**) and parent branches (**B**) in relation to their starting diameters (abscissae). The correlation between branch length and starting diameter was positive for terminating branches and negative for parents. The inset in panel **A** shows a histogram of branch taper, which had a mean of $-0.0007 \pm 0.0027 \mu\text{m}/\mu\text{m}$. Adapted with permission from Figure 1 in (20).

soma or a branch point and ending either at another branch point or at a termination (Fig. 2; see also Fig. 5 in [8]). As in most reconstructed neurons, the branches consisted of a sequence of segments, often with different diameters due to dendritic taper. Despite a great deal of scatter, the lengths of branches that ended at a branching point (called “parent” branches) varied inversely with their starting diameters, while the relation was direct in the case of terminating branches. It was also clear that the diam-

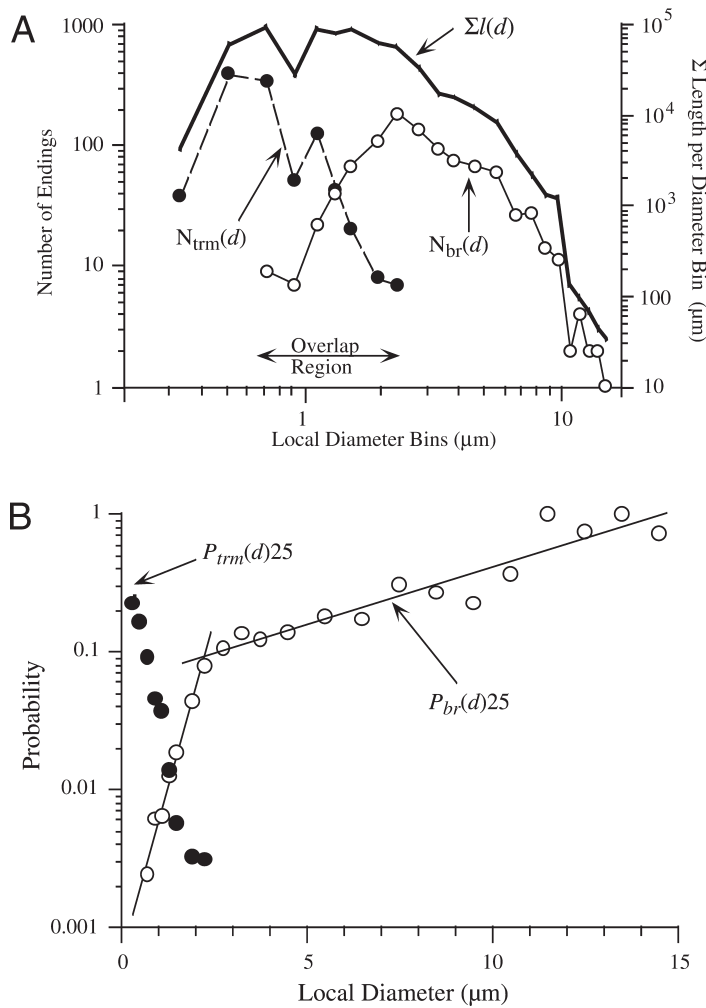


Fig. 3. Calculation of the probabilities of branching or termination as functions of local branch diameter [$p_{br}(d)$ and $p_{trm}(d)$, respectively]. (A) Log-log plot of the total length of dendritic material [$\Sigma l(d)$; solid line, referred to the right ordinate] and the numbers of branch segments giving rise to branching points [$N_{br}(d)$] or terminations [$N_{trm}(d)$], as functions of local diameter (d), binned by 0.25 μm for $d \leq 2.0$ μm, 0.5 μm for $d > 2.0$ to ≤ 4.0 μm, and 1.0 for $d > 4.0$ μm. Segments with diameters between 0.8 and 2.2 μm (overlap region) could either branch or terminate. (B) Semilog plot of the ratios of the numbers of branch points or termination, divided by $\Sigma l(d)$, to give $p_{br}(d)$ and $p_{trm}(d)$, respectively. In this graph, $p_{br}(d)$ and $p_{trm}(d)$ are multiplied by Δl of 25 μm, which was the value of Δl used for simulations. Adapted with permission from Figure 2 in (20).

eters of most individual branches became smaller in the somatofugal direction (i.e., they exhibited negative taper).

In order to simulate the wide scatter in branch lengths, which was as large for individual motoneurons as for the pooled data (Fig. 2), we used a stochastic (Monte Carlo) growth algorithm in which each increment in branch length, Δl , was controlled by the probability that it ended in a branching point or in a termination (p_{br} or p_{trm} , respec-

tively). If neither was true, the branch continued to lengthen by Δl . The observations suggested that both p_{br} and p_{trm} depend in some way on branch diameter. In order to explore this possibility, we binned all of the branch segments by increments of diameter, d , and summed the total length $\Sigma l(d)$ in each diameter bin (Fig. 3A). The numbers of segments in each diameter bin that ended in either a branch point, $N_{br}(d)$ or a termination, $N_{tr}(d)$, were then divided by $\Sigma l(d)$ to give $p_{br}(d)$ and $p_{trm}(d)$ per unit length as functions of local segment diameter bins:

$$p_{br}(d) = \frac{N_{br}(d)}{\Sigma l(d)} \quad \text{and} \quad p_{trm}(d) = \frac{N_{trm}(d)}{\Sigma l(d)}$$

As shown in Fig. 3B, the resulting probabilities [$p_{br}(d) \Delta l$ and $p_{trm}(d) \Delta l$ with $\Delta l = 25 \mu m$] were well fitted by exponential functions of local diameter, d , with positive exponents for $p_{br}(d)$ and negative for $p_{trm}(d)$. Within the range of d where branches either branched again or terminated (overlap region; $d = 0.7$ to 2), the slope for $p_{br}(d)$ was much steeper and approx the inverse of the slope for $p_{trm}(d)$ (2.2 vs -2.9 , respectively; see Table 1 in [30]).

To start the simulation process, the diameter of the first segment in the branch and a step length (Δl) are specified, and the computer compared p_{br} or p_{trm} , (multiplied by Δl and randomized as to which was tested first in order to eliminate bias) with a uniformly distributed random number, rnd between zero and 1. If this $p_x < rnd$, the branch ended appropriately. If neither event occurred, the branch extended by Δl , d_{i+1} changed by a selected value for taper ($\Delta d/\Delta l$), and the process was iterated until the branch either terminated or produced a branching point. The value of taper used was the only free parameter in the system, because it was difficult to specify a single value from the wide observed distribution (Fig. 2, inset). The algorithm produced parent and terminating branches with the observed length distributions (Fig. 2) with reasonable fidelity, given that a single value of taper was used for all branches. The value of taper that produced the least error in this simulation was $-0.00125 \mu m/\mu m$ (Fig. 5 in [20]), which was comparable with the observed value (Fig. 2A, inset), given that taper is extremely difficult to measure with any accuracy.

Of course, this was only half of the process required to produce virtual trees; one must also specify the diameters for the daughter branches that are generated when a parent branch gives rise to a branching point. In real motoneurons, the average ratio between the sum of the daughter branch diameters (d_1 and d_2), raised to the $3/2$ power, divided by the $3/2$ power of the parent diameter (d_{par}), is slightly larger than 1.0 (actually 1.1), but shows wide variations (see Fig. 7 in [12]). Like most neurons, branch points in motoneuron dendrites give rise to only two daughter branches, and their diameters are negatively correlated (Fig. 4A). This relation was independent of both position in the tree and the end diameter, d_{par} , of the parent branch.

The distributions of d_1 and d_2 were Gaussian and exhibited similar means and standard deviations (SD). One of us (W.B.M.) devised a way to combine their values, using their observed correlation coefficient $\beta = -0.4$, into a single distribution, r , which was well approximated by a Gaussian with the same mean and SD (Fig. 4B). Drawing two numbers independently from r , multiplying this pair by the matrix $\{\{1, -.2087\}, \{-.2087, 1\}\}$, and then by d_{par} produced a pair of daughter branch diameters that,

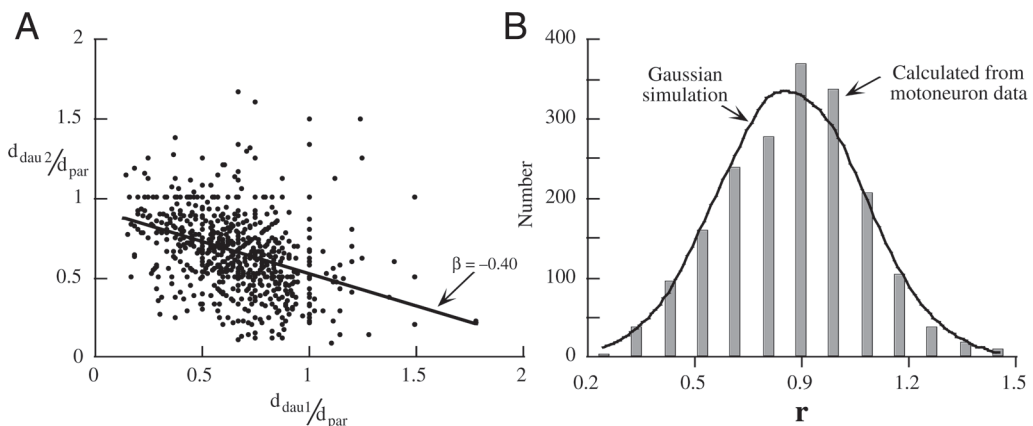


Fig. 4. Database for choosing diameters of daughter branches at simulated branch points. **(A)** Scatter plot showing the negative correlation between the diameters, d_1 and d_2 , of the two daughter branches at 955 branching points, each normalized by the end diameter of the parent branch. The slope of the linear correlation, $\beta = 0.40$, was used to construct a distribution, r , that preserved the statistical relations between d_1 and d_2 (see [20]). The value of β was the same whether or not the data were shuffled. **(B)** The calculated r distribution (bars) were fit to a Gaussian function (solid curve) with the same mean and SD. The continuous function was used for generating virtual dendrites (see [20]). Adapted with permission from Figure 6 in (20).

when repeated, had the same means, SDs, and correlation coefficient as the observed daughter branch diameters.

A program was written that combined the branch growth algorithm discussed above with the algorithm for determining daughter branch diameters in order to construct virtual dendrites with a selected starting diameter, d_{stem} , that matched diameters of observed dendrites. The experimental database included 64 fully reconstructed dendrites from 6 α -motoneurons, with d_{stem} ranging from 2 to 18 μm . Each run of the program generated 64 virtual dendrites, using parameters based on the probabilities shown in Figure 3B and the algorithm for selecting daughter branch diameters (Fig. 4B). The program automatically calculated a wide variety of statistics about virtual dendrites that could be compared to their actual counterparts (e.g., Figs. 5 and 6).

Twenty simulations were run for several values of taper and each produced dendrite sets with different total numbers of terminations, indicative of the overall size of the simulated trees. There was a direct relation between taper and total termination numbers, in that more negative values of taper produced smaller trees. The value of taper used was adjusted empirically to produce dendrite sets with total termination numbers near that observed for the real motoneurons ($n = 1974$). A taper value of -0.0015 produced the closest approach to this number but individual runs varied rather widely.

This model system, referred to as “Model 1”, produced virtual dendrites that matched many of the relations found in the actual database, including the distributions of total surface area and numbers of terminations in relation to d_{stem} for individual trees (see Fig. 7 in [20]) and the distributions of branch orders and diameters of parent and terminating branches as functions of distance from the soma (Fig. 5A, B, and D). None of

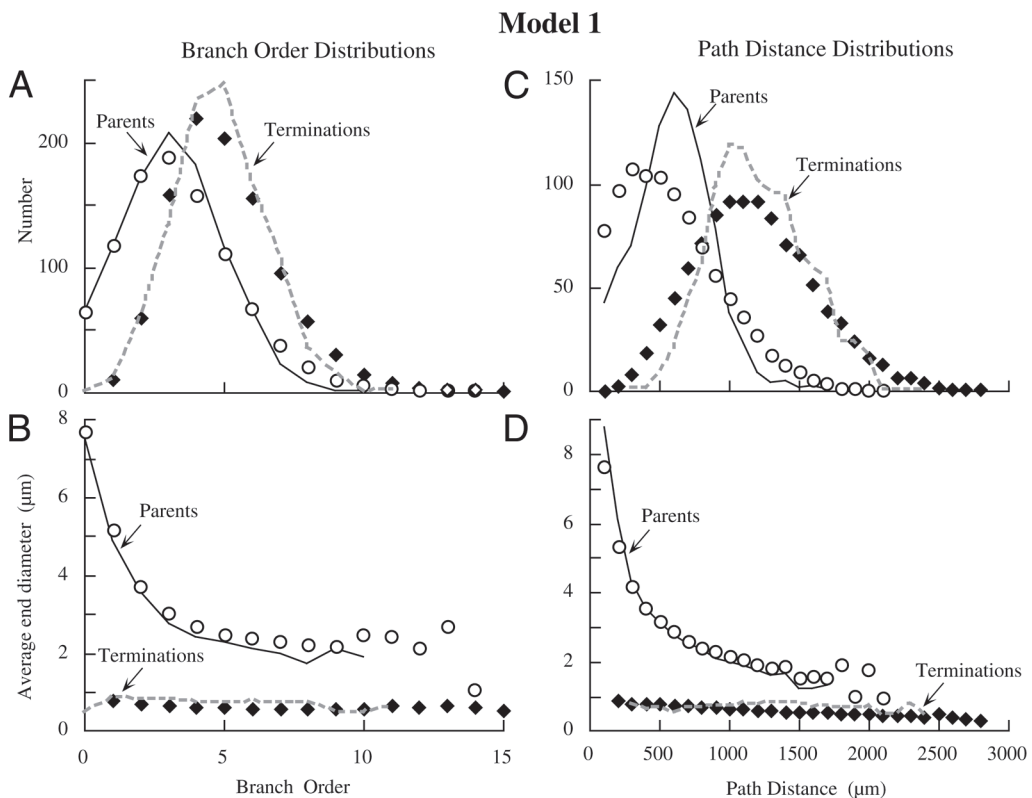


Fig. 5. Comparison of averaged data extracted from 64 simulated (symbols) and actual (lines) dendrites with the same set of stem diameters, using Model 1 simulations (see text). Note branches of order >10 in the simulations (**A** and **B**) and major discrepancies in the path distance locations of branch points and dendritic terminations (**C**). Adapted with permission from Figure 8 in (20).

these relations were built into the simulation algorithm; rather they are emergent properties that can serve as features for determination of goodness of fit. Although the path distance distributions of branch points and terminations were less satisfactory (Fig. 5C), this might be deemed good enough given the relative simplicity of the model.

This model result must be interpreted with caution. Although a growth model was used for these simulations in order to simulate the statistical variances in real dendrites, the results are a simulation of existing dendritic structures rather than of the dynamic processes that may have formed them. The computational machine and the parameters shown in Figures 3 and 4 should be thought of as a parsimonious description of the complex morphology of cat motoneuron dendrites that eliminates redundant information, rather than a model of how dendrites actually grow. Given this important distinction, the Model 1 results suggests that local branch diameter is a key factor that determines whether a given branch can or cannot maintain a branching point rather than terminating. This is consistent with the idea that the cytoskeleton, specifically the number of available microtubules (17), controls whether or not a given branch can give rise to a branching point, as well as how long parent and terminating branches can be.

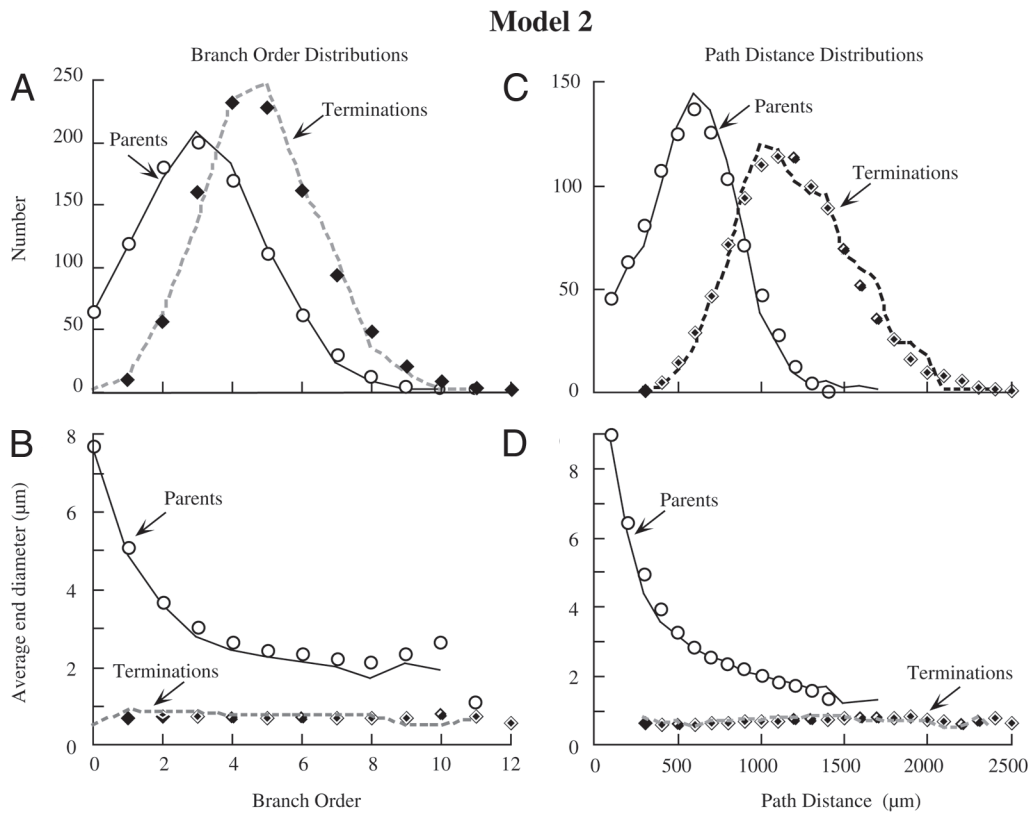


Fig. 6. As in Figure 5 but using Model 2 for simulations. Note lack of simulated dendrites with branch orders >11 (**A** and **B**) and much closer agreement between simulated and observed locations of branching points and terminations as functions of path distance from the soma (**C**). Adapted with permission from Figure 12 in (20).

An alternative model, in which p_{br} and p_{trm} were functions of branch order alone rather than local diameter, produced poor fits to the actual data. Thus, observed correlations between branch order and dendritic architecture are probably epiphenomena.

2.3. HOW GOOD IS GOOD ENOUGH?

One of the more difficult questions in any computational model study is when to quit. The failure of Model 1 to completely reproduce the spatial distributions of branch points and terminations (Fig. 5C) suggested that it lacked some important factor. In addition, some runs of this model produced trees that were either much smaller or much larger than expected for the selected value of d_{stem} . The existence of “runaway” dendrites is evident in Figure 5B, which shows diameters of parent and terminating branches with branch orders >10 that are not found in real motoneurons. The richness of the database prompted us to explore other factors that might have accounted for these discrepancies.

The problem of trees that were too small or too large appeared to be caused by sequences of daughter branch diameters that, in rare instances, were either very small

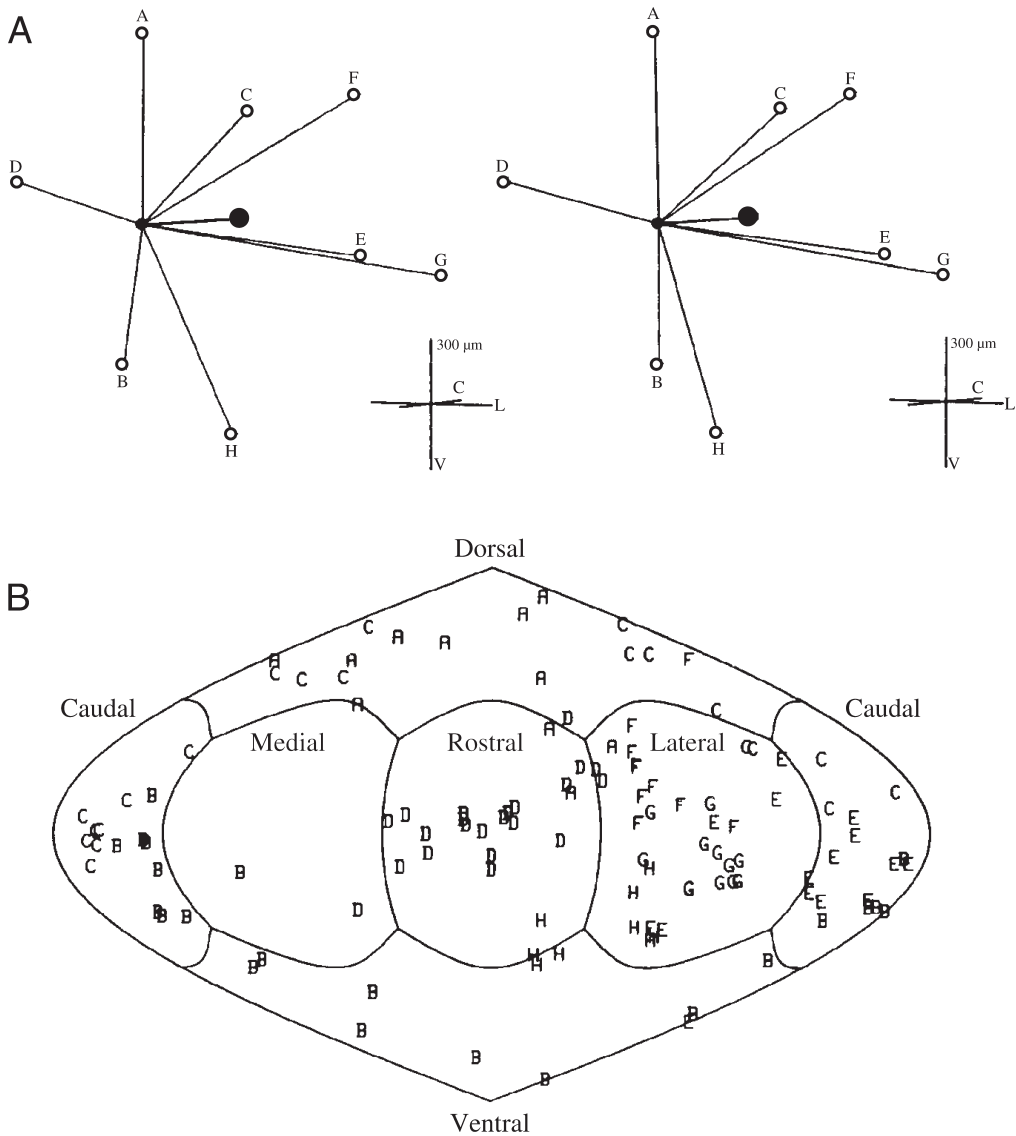


Fig. 7. Two simple approaches to quantitate the 3D morphology of a motoneuron. **(A)** Stereoscopic pair representation of the vectors of eight dendrites (labeled A through H) in terms of the centers of mass (open circles) of the membrane area in each dendrite, illustrating the projection of each dendrite away from the soma (small filled circles). The large filled circle represents the membrane area center of mass for the entire neuron. This was the most asymmetrical motoneuron of six similarly studied cells (26). **(B)** 2D projection of the locations at which dendritic branches of the same cell as in panel A penetrate a spherical shell with radius 750 μm, centered on the soma. Individual branches of the different dendrites are labeled with the dendrite identification letter. The lines indicate the boundaries of six directional hexants, with the caudal hexant split in two. The mapping projection assigns approximately equal areas to each hexant region. Both panels adapted from Figure 6 in (26).

or very large at successive branch points. This could occur by chance because the model had no memory of the preceding selections of d_1 and d_2 . When we reexamined the experimental data, we found a small but significant dependence between the sum of d_1 and d_2 at a given branch point, normalized by the parent end diameter, d_{par} , and the starting diameter of the parent branch, normalized by the end diameter of its parent branch (i.e., the “grandparent” branch). This suggested the existence of a cytoskeletal or metabolic constraint on the size of the downstream subtrees. We implemented a “grandparent correction” based on the observed dependence, and this greatly reduced the occurrence of runaway trees, but neither this nor several other manipulations improved the discrepancy noted in Figure 5C (see [20] for details).

Another reexamination of the original data suggested that the values of $p_{br}(d)$ and/or $p_{trm}(d)$ might not be constant throughout the tree. Indeed, we found that both probabilities depended on the path distance, D , from the soma as well as on local diameter. Such a dependence could represent the metabolic cost of maintaining cytoskeleton at increasing distances away from the soma where the constituent proteins are generated. Estimation of this dependence was complicated by the problem of fitting smooth functions to the 3D surface described by the data points, now binned by both local diameter and path distance (see Fig. 10 in [20]). However, when equations for $p_{br}(d, D)$ and $p_{trm}(d, D)$ that fit the data were incorporated into the model, it produced trees that fit the observed data very well indeed (Fig. 6). It was necessary to analyze the data for dependence on d and D separately, because local diameters in individual branches were not strongly correlated with path distance, especially in the more distal parts of the trees (Fig. 1). These virtual dendrites also had branch topologies that fit those of actual motoneuron (Burke, Marks, and Ulfhake, unpublished). In this instance, all of the required parameters were intrinsic to the neuron itself. This may not always be true; in some cases external factors could be required in order to generate acceptable simulations (e.g., [22]).

The lesson for us in this work was that it is sometimes useful to extend a model that is reasonably good to one that is better, provided that the additions accurately reflect features that are in fact present in the original data. Each elaboration of the present model revealed factors that appear to be biologically relevant. The additional features were not at all obvious and emerged only after specifically tailored data extraction methods were employed. Indeed, the utility of quantitative biological models lies precisely in the fact that they force the investigator to search for relations that are hidden within the existing data or to guide the experiments that can generate the necessary new information.

2.4. NEURONS IN THREE DIMENSIONS

2D morphological data are relatively tractable for computational modeling, as exemplified by the discussion so far. However, it is considerably more difficult to extend such approaches to neurons as 3D entities (17). The overall shape of neuronal dendritic trees have been analyzed by statistical methods, such as principle components (23,24), and by a Fourier transform technique that can give concise information about the density of branches distributed in 3D space (25). Cullheim and colleagues (26) introduced a simpler approach that tabulated the spatial distribution of the dendritic membrane

area or branch volume within six “hexants”, or subdivisions thereof, within an external coordinate system centered on the neuron soma and oriented by anatomical axes. These authors also used a variation of principle component approach to calculate the spatial locations of the centers of mass (COM) for membrane area or branch volume for individual dendrites, as well as for the neuron as a whole (Fig. 7A). On average, cat triceps surae motoneurons were found to be more or less radially symmetrical, although the dendrites projecting dorsally and ventrally tended to be slightly smaller than those that projected in the other directions. All of these methods provide ways to document the degree to which neuronal trees are polarized, either because of proximity to natural boundaries or, perhaps, to concentrated sources of synaptic input.

Another approach to the problem of analyzing the 3D spatial organization of dendrites is to map the spatial positions of their branches as they penetrate 2D spherical surfaces (“shells”) located at different distances from the soma (Fig. 7B; [26]). Although such shell maps are on spherical surfaces, they are tractable for quantitation by spherical trigonometry. Questions such as the size of dendritic territories and how much they overlap can be approached by conventional nearest-neighbor or tessellation analyses to examine spatial clustering. Convex hulls (polygons with no internal angle $< 180^\circ$ that encloses the target set of points) are computationally convenient, although they often include empty regions that properly belong to other dendrites. The disadvantage of such maps is that they do not lead to simplification of the data set or to identification of general principles that might be at work.

2.4.1. Building Three-Dimensional Dendrites

Renewed interest in computational neuroanatomy (21), as well as the appearance of relevant software tools (27,28), has stimulated the development of new approaches to quantitate neuronal morphology in 3D space that involve simulation. In an earlier section, we adopted the view that the simplest computational machine that can accurately reproduce a set of complex objects constitutes the most concise description of those objects. This philosophy predicts that new information may emerge if we can construct algorithms that can convert 2D dendrograms into statistically accurate 3D trees. At minimum, such a simulation requires extraction of two sets of data from the original morphological files: (i) the distributions of angles at which daughter branches emerge from branching points; and (ii) measurement of the degree to which individual branches meander (i.e., change in vectorial orientation) in space (8). In principle, these data can be estimated from cells that have been digitized with sufficient spatial resolution.

As an example, we will consider here some possible approaches to measurement of daughter branch angles. The first decision is how to define the vectorial directions of daughter branches away a given branching point. There are at least three possibilities: (i) use the coordinates of the first digitized segment of each daughter branch (initial branch direction); (ii) use the coordinates of the point at which the branch ends (final branch direction); or (iii) use the least-squares fit to each meandering branch, perhaps weighted by local membrane area or segment volume (average branch direction). Because we were interested in the global shape of trees, we initially used the final branch directions.

The next issue is to define the frame of reference for measuring branch angles. An obvious choice is to calculate angular deviations from the parent branch direction.

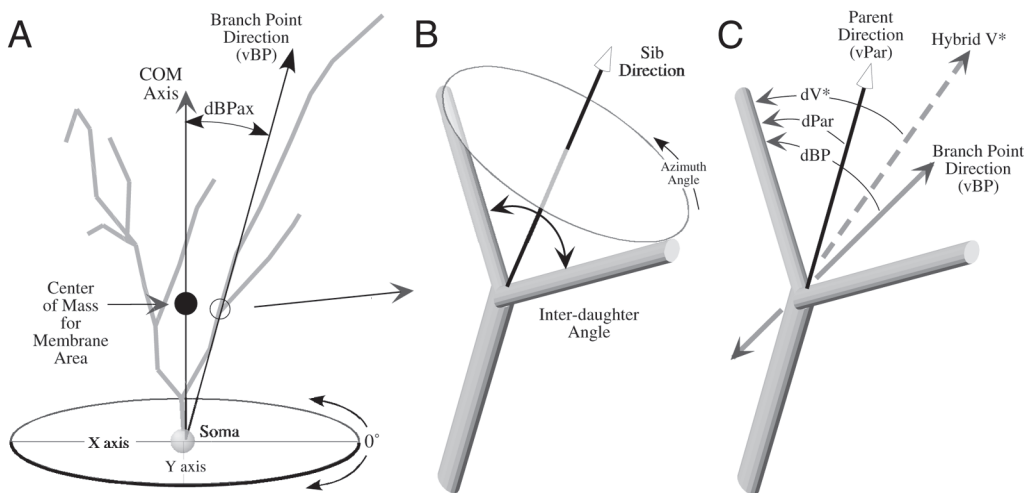
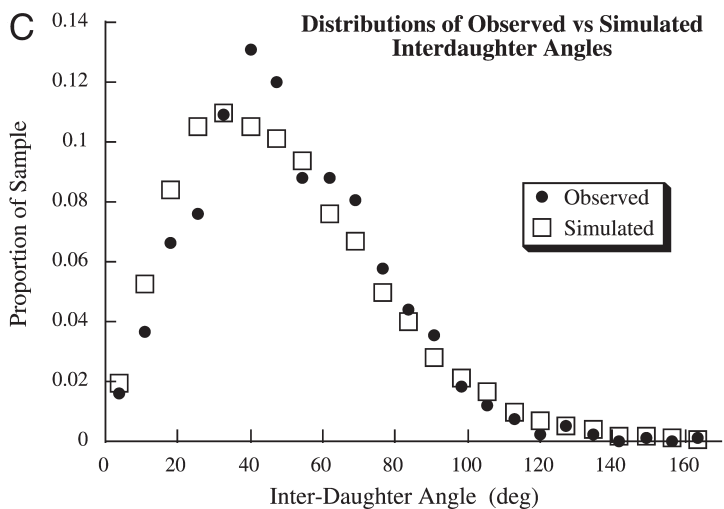
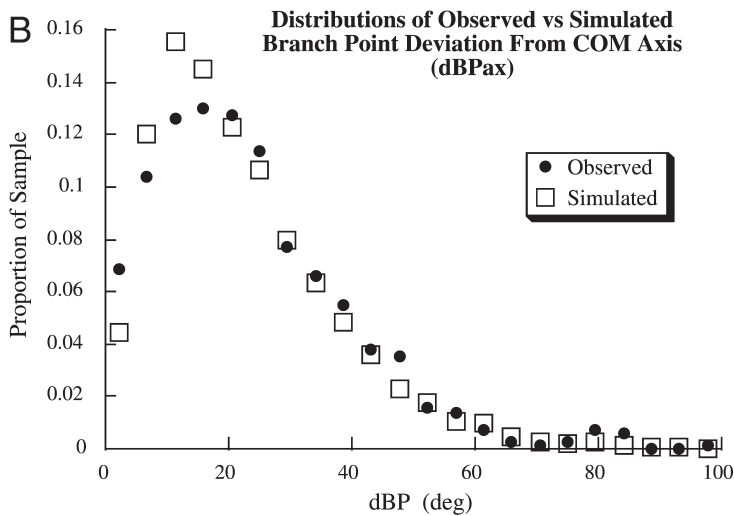
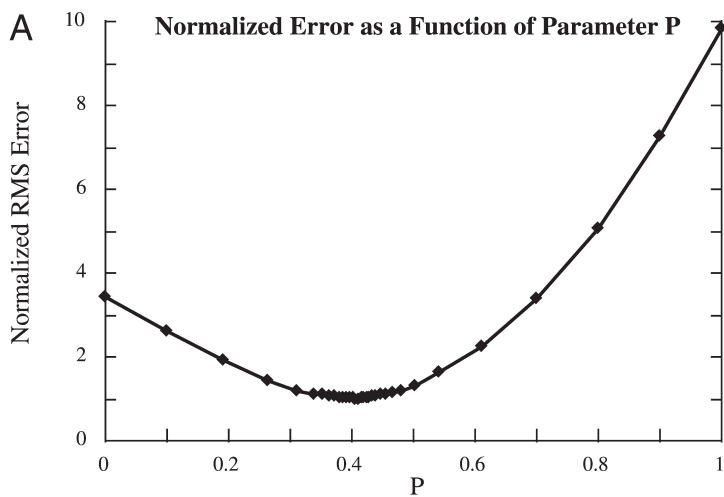


Fig. 8. Diagram to illustrate possible methods to calculate dendritic branching angles. **(A)** A motoneuron dendrite is shown after rotation into a Cartesian coordinate space, aligned in the Z (vertical) axis by the vector from the soma center to the COM for dendritic membrane area (filled circle). The direction of each branch point with respect to the COM axis can be specified by its dBPax away from the COM axis. Its horizontal position is described by an azimuth angle in the XY plane with respect to a reference direction (e.g., rostral). **(B)** The orientation of daughter branches at each branch point can be described by the angle between them (Interdaughter angle) and the vector midway between them (Sib direction). The Sib vector can be viewed as the axis of a cone around which the daughter branches can rotate in the perpendicular (azimuth) plane. **(C)** The direction of the individual daughter branches can be defined as the angle of deviation away from the branch point direction (dBP) or the direction of the parent branch (dPar). The most successful 3D simulations were obtained when daughter branch deviation angles (dV*) were referenced to a vector representing a linear combination of the branch point and parent directions (Hybrid V*; see text).

However, a 3D simulation algorithm, based on parent branch vectors, produced simulated trees that often had much larger lateral spread than natural cat motoneuron dendrites (Burke and Marks, unpublished), because such data has no relation to the shape of the tree as a whole. In fact, it can be shown that using only the parent branch direction leads to a 3D random walk. As discussed in the chapter by Ascoli (see also [27,28]), this can be overcome by introducing a spatial bias, or “tropism”, to constrain tree growth in specified directions, but the underlying factors that produce such effects are unclear. We attempted to determine whether such biases are inherent in the statistics of the spatial disposition of branch points and path terminations in relation to a global frame of reference for a given tree.

In order to define a central axis for each individual dendrite, we chose to use the vector from the center of the soma to the COM for membrane area (Fig. 8A; [26]). The somatofugal COM axis was aligned with vertical (Z) axis of a Cartesian coordinate system, just as botanical trees are oriented with respect to gravity (29,30). The location of each branch point (BP) in the tree was then specified by its angular deviation (dBPax)



away from the COM axis and its azimuth angle in the XY plane (Fig. 8A). The distribution of dBPax angles provides a concise measure of the lateral dispersion of the dendrite's territory (see Fig. 9B).

We then needed a scheme for specifying the angular deviations of daughter branches at BPs that could serve as the basis for a simulation algorithm for 3D trees. Such a system should make maximum use of local frames of reference, as in the 2D models described above. We found it initially useful to define the direction of branching by calculating a "Sib" vector midway between the two daughter branches that represents the axis of a cone around which daughter branches, with any given interdaughter angle, can rotate into any azimuthal orientation (Fig. 8B). As with the azimuth angles of BPs, these orientations showed no rotational bias in motoneuron dendrites, so they can be evenly distributed in simulations. Still open is the question of what vector to use in measuring the Sib deviation. Using the parent branch direction alone again leads to a spatial random walk. However, using the direction of the branch point vector (vBP) defined in relation to the COM axis (Fig. 8A) preserves information about global tree structure. The azimuth of the Sib about this direction also turned out to be unbiased. Thus, two distributions, one for the Sib deviation and the other for interdaughter angle, provided the basis for a 3D simulation algorithm. Both distributions were well fitted by Δ functions, each specified by two parameters, that are easily adapted for Monte Carlo simulations. Of course, the eventual COM axis of a simulated tree is unknown at the outset of 3D simulation, so we used the Z axis of the Cartesian frame as the reference vector.

We also explored a simpler algorithm that used only the distribution of deviations of the individual daughter branch directions (vDau) at each branching point as the basis for building complete trees. This approach was complicated by the fact that vDau was correlated with both vBP as well as with the direction of the parent branch (vPar) (Fig. 8C). The distributions of angular deviation between vDau and either vBP or vPar (dBP and dPar, respectively, in Fig. 8C) were both well-fitted by Δ distributions. As expected from the Sib data discussed above, neither vector exhibited any bias in azimuth orientation. Complete trees for 60 individual dendrites were simulated using either the dBP or the dPar distributions, based on length and diameter data from 60 real motoneurons. The total root mean square (RMS) error between a variety of angular measures

Fig. 9. (facing page) Results of simulating the 3D structure of 60 motoneuron dendrites. **(A)** Plot of RMS errors in 3D simulations based on using different proportions (P) of the branch point and parent directions [$V^* = (1 - P) vBP + P vPar$] to calculate dV*. Simulations based entirely on the observed distribution of dBP (P = 0) produced less error than those based entirely on dPar (P = 1), but minimum error was found with P ~ 0.4. See text for details. **(B)** Comparison of the distributions of the angular deviation of branch points away from the COM axis (dBPax; see Fig. 8A) in 60 actual dendrites (filled circles) and averaged values from 10 repetitions of 3D simulation of the same 60 trees (open squares). Simulations used the distribution of daughter branch deviations, dV*, from the Hybrid vector, V*, with P = 0.4. The fit between the two distributions of the emergent property dBPax indicates that the real and simulated dendrites have the same (statistical) lateral spread. **(C)** As in panel B, but showing the comparison of real and simulated interdaughter angles. Interdaughter angle is also an emergent property, because the daughter branch directions are simulated separately and independently.

for simulated and real trees was smaller in the set of trees constructed using the dBP distribution (Fig. 9A; error = 3.4% with $P = 0$) as compared to the set simulated using the dPar distribution (Fig. 9A; error = 9.9% with $P = 1$). We then explored using a hybrid vector (V^*) calculated as a linear combination of the branch point and parent directions (vBP and vPar, respectively)

$$V^* = (1 - P) \text{vBP} + P \text{vPar}$$

as the reference vector to calculate the deviation (dV^*) for each daughter branch (Fig. 8C.). As with the Sib vector approach above, V^* can be viewed as the axis of a cone that describes the locus of the distribution of daughter branch directions.

With simulations based on the dV^* distribution, the overall RMS error for the 3D tree statistics were minimal with $P \sim 0.4$ (Fig. 9A). Furthermore, the distribution of angular deviations of branch points away from the COM axis (dBPax; Fig. 8A), as well as the interdaughter angles, for the simulated trees matched the observed data quite well (Fig. 9B and C). The azimuthal angles for daughter branch directions in the XY plane also matched those of real trees (not shown). These 3D statistical measures are emergent properties that are not specified by the simulation algorithm, so that the fits indicate that the simulation accurately reproduced the overall 3D structure of motoneuron dendrites with straight branches. The simulated trees exhibited the same range of constraint in lateral spread as real dendrites (estimated by dBP; Fig. 9B), and their overall shapes appeared appropriate to visual inspection. The final 3D algorithm used only three parameters, two to specify the Δ function that fits the daughter deviations from V^* , plus the minimum error value of $P = 0.4$. This result suggests that the spatial distribution of daughter branches in motoneuron dendrites can be described by factors related to the central axis of the tree, which could reflect environmental constraints, and, to a lesser extent, on purely local factors related to the direction of the parent branch. We are investigating an analogous approach to simulation of the natural mean-der of individual branches.

A more difficult problem for simulation of dendritic trees in 3D is that multiple objects cannot occupy the same point in space. There may even be some active avoidance among branches from the same neuron (31). Adjustment of the 3D positions of simulated dendrite branches would probably best be accomplished after the complete structure has been constructed. Ideally, such adjustments should be based on data from real dendrites that give information on the spacing between their components. To our knowledge, such analyses have not been made with *in situ* neuronal dendrite data, although some basic theoretical solutions to the problem have been suggested (32).

In the same vein, simulation of the complete dendritic tree of a single multipolar neuron will require regional analysis of the positions of all elements, beginning near the soma. Although it is simple to arrange the COM vectors of simulated trees to project away from each other, the possibility of unnatural collisions exists after the first branch points. Any spatial adjustments to a given element made near the soma would propagate outward, presenting a potentially massive computational problem. It is tempting to sidestep this problem by simply accepting 3D virtual neuron simulations that subjectively appear “natural.” However, it seems important for the field to develop objective assessments that could reveal important constraints that remain unresolved at present.

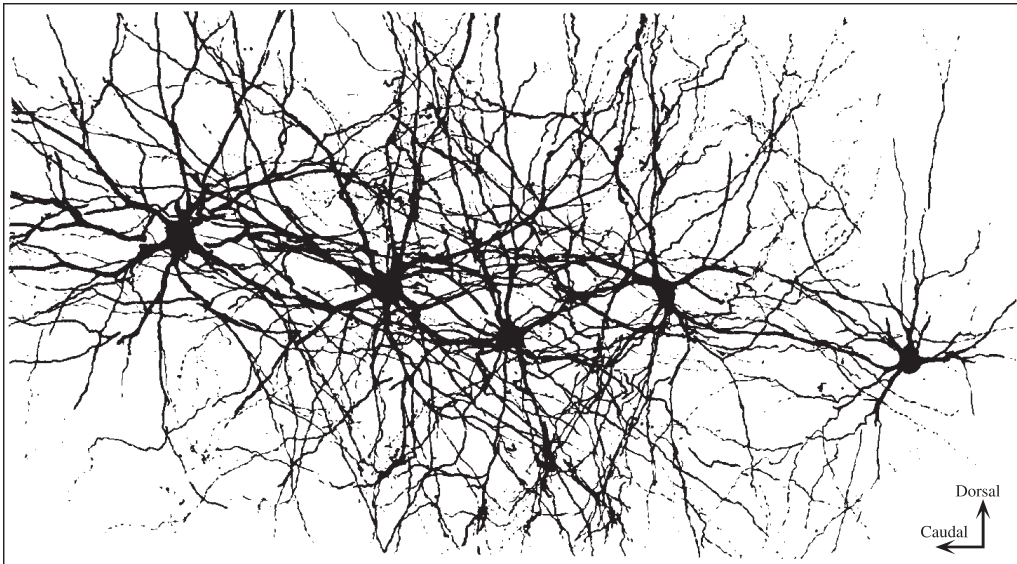


Fig. 10. Photomontage from three serial sagittal sections showing the somata and portions of the proximal dendritic trees of 5 filled α -motoneurons from a cat spinal cord. Note the complex interweaving of the trees from different cells. The somata are about 50 μm in diameter. Adapted from Figure 18 in (41).

2.4.2. The Problem of Neuronal Packing

Clearly, accurate simulation of the 3D structure of individual neurons is a formidable problem. It is at least as difficult to devise quantitative approaches that can be used to measure how multiple neurons with overlapping dendritic territories are packed into the neuropil. The neuropil must provide space not only for somata, dendrites, and the synaptic boutons associated with them, but also for axons with and without myelin sheaths, glia, blood vessels, and extracellular space. Stereological methods can provide estimates of numbers of neurons (33) and the volume fraction occupied by these elements (34). However, such data do not provide a clear picture of how individual neurons with extensive dendritic trees can share a given volume of neuropil. The complexity of this problem is illustrated in Figure 10, which shows the intermingled dendritic trees of just 5 HRP-labeled α -motoneurons that undoubtedly share this volume with many unlabeled cells.

We have looked at one approach to this problem using existing data to get estimates of the 3D volume fractions occupied by the dendritic trees of cat motoneurons, plus the synaptic boutons on them, as functions of radial distance from the soma. These estimates were used to explore the consequences of motoneuron packing density on the composition of the neuropil between the cells. Lumbosacral motoneurons in the central part of the ventral horn are, on average, radially symmetrical (3,26), so that the same volume fraction function can be used for all directions. The average surface area and volume (expressed as percent) of the dendrites of 7 α - and 11 γ -motoneurons (12,26,35) were calculated within successive 100- μm -thick spherical shells centered on the soma

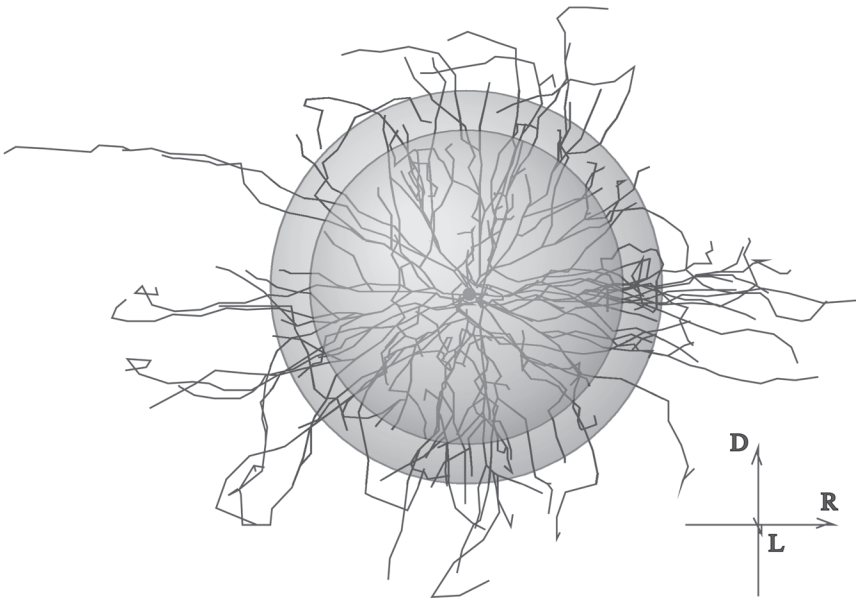


Fig. 11. 2D drawing of a completely reconstructed cat α -motoneuron superimposed on two spheres that represent different radial distances from the center of the soma. The volume between the spheres (“shell volume”) contains elements of the dendritic tree, permitting calculation of the volume fraction occupied by elements of the neuron. The direction arrows are 500 μm long.

(Fig. 11). Similarly, we estimated the volume of the associated synaptic boutons in each shell, based on postsynaptic surface area distributions plus data about synaptic covering and bouton size data for cat α - (36) and γ -motoneurons (37). The sum of dendritic and bouton volume, when divided by the total volume in each concentric shell, gave estimates of the average volume fraction within each radial shell that is occupied by each type of neuron plus its synaptic boutons (expressed as percent; symbols in Fig. 12A). The solid lines are fits to these data using the following equation:

$$V_{fr} = \gamma \left(\frac{\beta}{d} - 1 \right)^\alpha$$

where α , β , and γ are fitting parameters and d is radial distance from the center of the soma.

Assuming that a motor nucleus in the ventral horn includes 65% α - and 35% γ -motoneurons (38), the fitted functions in Figure 12A were combined in those proportions to give the average volume fraction occupied by both types of motoneuron in the cat ventral horn. Because motoneuron dendrites are so extensive (up to 2000 μm from the soma), cells located at considerable distances from any given motoneuron can contribute to the neuropil in the center of the ventral horn. In order to evaluate the total volume fraction contributed by such overlapping dendrites and synaptic boutons, we assumed (for computational simplicity) that motoneurons are arranged in a cubic matrix with the separation (S) between somata as a free variable. A program was written in

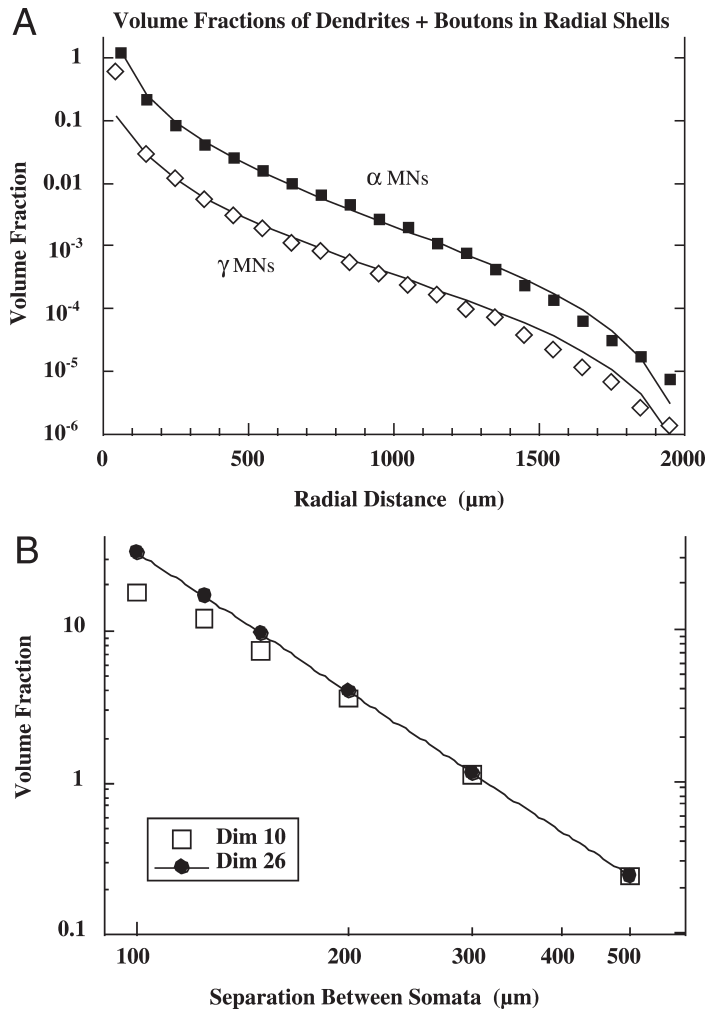


Fig. 12. Estimation of volume fraction occupied by motoneurons and associated synaptic boutons in the cat ventral horn. **(A)** Semilog graph of the estimated volume fractions (symbols) occupied by the dendrites and associated synaptic boutons of average α - (filled squares) and γ -motoneurons (open diamonds), calculated as described in the text. The calculated data were fitted with the equation given in the text. **(B)** Log-log graph showing the total volume fraction (ordinate, in percent) occupied by dendrites and boutons within the open central cube of a cubic array of ventral horn neurons with a uniform separation distance, S (abscissa), when calculated with different numbers of cells along each matrix edge (Dim). See text for further explanation.

MatLab[®] to calculate the average local volume fraction (V_{fr}) of dendrites plus boutons within the open cube at the center of the cell matrix. This was done by randomly sampling 100 locations within the central cube for various values of S . The log-log graph in Figure 12B illustrates how V_{fr} depends on S , as well as on the size (Dim) of the cell matrix, where Dim is the number of somata along each side of the cubic matrix.

When Dim was large enough so that the dendrites of cells along the edges could reach the central cube even with relatively small S ($Dim = 26$), V_{fr} (in percent) varied as

S^3 . With smaller matrix dimensions ($Dim = 10$), V_{fr} departed from this power relation as S decreased, because the array limits were smaller than the dendrite extensions from the most peripheral cells. Although estimates of V_{fr} occupied by dendrites and boutons are not available for the cat ventral horn, such estimates from medial lamina VI in the rat spinal cord (34) suggest that dendrites and synaptic boutons occupy about 16 – 20% of the neuropil volume in lamina VI. The dimensions in the actual cat ventral horn are compatible with Dim between 10 and 26, so that this analysis suggests that V_{fr} would be between 11 and 18% for $S = 125 \mu\text{m}$ (Fig. 12B). From the numbers and positions of motoneuron somata found in the lumbosacral ventral horn of the cat (Fig. 2 in [38]), we estimate that their average separation is about $125 \mu\text{m}$ (see also [39]). The fairly good agreement from these independent estimates suggests that this approach may be a valid way to get quantitative estimates of neuropil sharing when the required data are available. Of course, this calculation assumed an isotropic neuropil and other geometries would require more complex algorithms.

2.5. CONCLUDING COMMENTS

This chapter has dealt with some approaches to the problem of quantifying the morphology of individual neurons and of ensembles of neurons, using data from cat ventral horn motoneurons. The ability to mimic the statistical properties of cat motoneuron dendrites, viewed in terms of their 2D dendrograms, using a relatively simple growth model based on data extracted from the same data set, provides a parsimonious description of the original data, which separates factors that are determinative from those that are epiphenomena. The result suggests that local branch diameter, which in large measure depends on cytoskeleton (8,17), is a key factor that maintains the architecture of mature dendrites. On the other hand, it is much more difficult to design computational engines that can reproduce the morphology of neuronal dendrites as 3D entities in ways that can be quantitatively verified. This is largely due to the difficulty of designing analytical tools that can adequately measure how these complex structures occupy space. One future direction for computational neuroanatomy is to solve this problem for individual neurons and then to apply the solution to multiple neurons that occupy the same region. This quest is more than an intellectual exercise, because the ability to simulate complex systems and to check the results of such simulation against the real thing has always led to deeper understanding of the biological world (40).

REFERENCES

1. Stuart G, Spruston N, Häusser M. (eds.) Dendrites. Oxford University Press, New York, 1999, pp. 376.
2. Cajal S. Histology of the Nervous System of Man and Vertebrates. (translated by Swanson N, Swanson LW) Oxford University Press, New York, 1995.
3. Ramon-Moliner E. An attempt at classifying nerve cells on the basis of their dendritic patterns. J Comp Neurol 1962; **119**:211–227.
4. Cullheim S, Kellerth J-O. Combined light and electron microscopical tracing of neurons, including axons and synaptic terminals, after intracellular injection of horseradish peroxidase. Neurosci Lett 1976; **2**:307–313.
5. Snow P, Rose P, Brown A. Tracing axons and axon collaterals of spinal neurons using intracellular injection of horseradish peroxidase. Science 1976; **191**:312–313.

6. Glaser E, Van der Loos H. A semiautomatic computer microscope for the analysis of neuronal morphology. *IEEE Trans Biomed Eng* 1965; **12**:22–31.
7. Johnson E, Capowski J. A system for the three-dimensional reconstruction of biological structures. *Comput Biomed Res* 1983; **16**:79–87.
8. Hillman D. Neuronal shape parameters and substructures as a basis of neuronal form. In: *The Neurosciences. Fourth Study Program* (Schmitt FO, Worden FG, eds.) MIT Press, Cambridge, MA, 1979, pp. 477–498.
9. Cline HT. Development of dendrites. In: *Dendrites* (Stuart G, Spruston N, Häusser M, eds.) Oxford University Press, New York, 1999, pp. 35–67.
10. Segev I, Burke RE, Hines M. Compartmental models of complex neurons. In: *Methods in Neuronal Modeling* (Segev I, Koch C, eds.) MIT Press, Cambridge, MA, 1997, pp. 93–136.
11. Sholl D. Dendritic organization in the neurons of the visual and motor cortices of the cat. *J Anat* 1953; **87**:387–401.
12. Cullheim S, Fleshman JW, Glenn LL, Burke RE. Membrane area and dendritic structure in type-identified triceps surae alpha-motoneurons. *J Comp Neurol* 1987; **255**:68–81.
13. Ulfhake B and Kellerth J-O. A quantitative light microscopic study of the dendrites of cat spinal α -motoneurons after intracellular staining with horseradish peroxidase. *J Comp Neurol* 1981; **202**:571–584.
14. Dityatev A, Chymykhova N, Studer L, Karamian O, Kozhanov V, Clamann H. Comparison of the topology and growth rules of motoneuronal dendrites. *J Comp Neurol* 1995; **363**:505–516.
15. van Veen M, van Pelt J. A model for outgrowth of branching neurites. *J Theor Biol* 1992; **159**:1–23.
16. Verwer R, van Pelt J. Descriptive and comparative analysis of geometrical properties of neuronal tree structures. *J Neurosci Methods* 1986; **18**:179–206.
17. Hillman D. Parameters of dendritic shape and substructure: intrinsic and extrinsic determination? In: *Intrinsic Determinants of Neuronal Form and Function* (Lasek RJ, Black MM, eds.) Alan R. Liss, New York, 1988, pp. 83–113.
18. Stevens J, Trogadis J, Jacobs J. Development and control of axial neurite form: a serial electron microscopic analysis. In: *Intrinsic Determinants of Neuronal Form and Function* (Lasek RJ, Black MM, eds.) Alan R. Liss, New York, 1988, pp. 115–145.
19. Tamori Y. Theory of dendritic morphology. *Phys Rev E* 1993; **48**:3124–3129.
20. Burke RE, Marks WB, Ulfhake B. A parsimonious description of motoneuron dendritic morphology using computer simulation. *J Neurosci* 1992; **12**:2403–2416.
21. Ascoli GA. Progress and perspectives in computational neuroanatomy. *Anat Rec* 1999; **257**:195–207.
22. Carriquiry AL, Ireland WP, Kliemann W, Uemura E. Statistical evaluation of dendritic growth models. *Bull Math Biol* 1991; **53**:579–589.
23. Brown C. Neuron orientations: a computer application. In: *Computer Analysis of Neuronal Structures* (Lindsey RD, ed.) Plenum Press, New York, 1977, pp. 177–188.
24. Yelnik J, Percheron G, François C, Burnod Y. Principle component analysis: a suitable method for the 3-dimensional study of the shape, dimensions and orientation of dendritic arborizations. *J Neurosci Meth* 1983; **9**:115–125.
25. Lindsey RD. Neuronal field analysis using Fourier series. In: *Computer Analysis of Neuronal Structures* (Lindsey RD, ed.) Plenum Press, New York, 1977, pp. 165–175.
26. Cullheim S, Fleshman JW, Glenn LL, Burke RE. Three-dimensional architecture of dendritic trees in type-identified alpha-motoneurons. *J Comp Neurol* 1987; **255**:82–96.
27. Ascoli GA, Krichmar JL. L-neuron: a modeling tool for the efficient generation and parsimonious description of dendritic morphology. *Neurocomputing* 2000; **32–33**:1003–1011.
28. Ascoli GA, Krichmar JL, Scorcioni R, Nasuto SJ, Senft SL. Computer generation of anatomically accurate virtual neurons. *Anat Embryol* 2001; **204**:283–301.

29. Ford R, Ford ED. Structure and basic equations of a simulator for branch growth in the *Pinaceae*. *J Theor Biol* 1990; **146**:1–13.
30. Honda H. Description of the form of trees by the parameters of the tree-like body: effects of the branching angle and the branch length on the shape of the tree-like body. *J Theor Biol* 1971; **31**:331–338.
31. Li GH, Qin CD, Wang ZS. Neurite branching pattern formation—modeling and computer simulation. *J Theor Biol* 1992; **157**:463–486.
32. Meyer F. Mathematical morphology: from two dimensions to three dimensions. *J Microscopy* 1992; **165**:5–28.
33. West MJ. Stereological methods for estimating the total number of neurons and synapses: issues of precision and bias. *Trends Neurosci* 1999; **22**:51–61.
34. Tredici G, Tarelli L, Cavaletti G, Marmiroli P. Ultrastructural organization of lamina VI of the spinal cord of the cat. *Neurobiology* 1985; **24**:293–331.
35. Moschovakis AK, Burke RE, Fyffe REW. The size and dendritic structure of HRP-labeled gamma motoneurons in the cat spinal cord. *J Comp Neurol* 1991; **311**:531–545.
36. Brännström T. Quantitative synaptology of functionally different types of cat medial gastrocnemius alpha-motoneurons. *J Comp Neurol* 1993; **330**:439–454.
37. Destombes J, Horschelle-Bossavit G, Thiesson D, Jami L. Alpha and gamma motoneurons in the peroneal nuclei of the cat spinal cord: An ultrastructural study. *J Comp Neurol* 1992; **317**:79–90.
38. Burke RE, Strick PL, Kanda K, Kim CC, Walmsley B. Anatomy of medial gastrocnemius and soleus motor nuclei in cat spinal cord. *J Neurophysiol* 1977; **40**:667–680.
39. Aitken JT, Bridger JE. Neuron size and neuron population density in the lumbosacral region of the cat's spinal cord. *J Anat* 1961; **95**:38–53.
40. Thompson D. *On Growth and Form*. Cambridge University Press, Cambridge, UK, 1942.
41. Burke RE. Motor units: anatomy, physiology and functional organization. In *Handbook of Physiology*, Sect. 1: The Nervous System, Vol. II. Motor Control, Part 1 (Brooks VB, ed.) American Physiological Society, Washington, DC, 1981, pp. 345–422.



<http://www.springer.com/978-1-58829-000-7>

Computational Neuroanatomy

Principles and Methods

Ascoli, G.A. (Ed.)

2002, XIII, 469 p., Hardcover

ISBN: 978-1-58829-000-7

A product of Humana Press